

Design and investigation of absolute radiance calibration primary radiometer

ISSN 1751-8822

Received on 15th September 2017

Revised 17th April 2018

Accepted on 09th July 2018

E-First on 24th September 2018

doi: 10.1049/iet-smt.2018.5127

www.ietdl.org

Ye Xin^{1,2}, Yi Xiaolong¹, Fang Wei¹, Wang Kai¹, Luo Yang¹, Xia Zhiwei¹, Wang Yupeng¹ ✉¹Changchun Institute of Optics, Fine Mechanics and Physics, Chinese Academy of Sciences, Changchun 130033, People's Republic of China²University of Chinese Academy of Sciences, Beijing 100049, People's Republic of China

✉ E-mail: wangyp@ciomp.ac.cn

Abstract: In order to satisfy the requirement of calibration precision and traceability for space remote sensor, the absolute radiance calibration primary radiometer (ARCPR) is investigated for establishing the irradiance calibration standard in orbit. ARCPR is a mechanical cryogenic absolute radiometer for space application, and works at 20 K. The cryogenic environment is obtained by the Stryn-type pulse tube cryocooler. The environment temperature is stable at 23.9658 K by high-precision temperature controllers. The detector of ARCPR is designed and investigated based on the experimental prototype. The experimental results of detector characteristics measurement illustrate that the sensitivity is 3.9526 K/mW, and the thermal time constant is 134 s. The procedure of optical power measurement is optimised for satisfying the requirements of in orbit measurement. ARCPR achieves a relative standard uncertainty of 210 ppm at an optical power level of 0.4 mW. Therefore, ARCPR could be the radiometric standard for optical measurement. Furthermore, the investigation result provides the theoretical and experimental basis for the establishment of radiometric calibration standard in orbit.

1 Introduction

The radiometric calibration is significant for manufacturing the space remote sensor [1, 2]. Radiometric calibration accuracy has a direct bearing on the quality of remote sensing data [3, 4]. The radiometric calibration methods are mainly divided into laboratory calibration and in orbit calibration. Based on higher stability light sources and standard transfer detectors, the laboratory calibration can achieve very high accuracy. However, affected by the launching process and the abominable space environment, the credibility of laboratory calibration result is lower. Therefore in orbit calibration is necessary for space remote sensor. Currently, the principles of in orbit calibration method are based on standard sources or site substitution. The accuracies of in orbit calibration methods are only 3 to 10%. Meanwhile, the radiation scale of in orbit calibration cannot be traced to the international unit system (SI) [5, 6]. Thus, the urgent requirement of in orbit radiometric calibration accuracy cannot be satisfied. Referring to the development trend of the ground radiometric calibration standard [7–9], the new method of in orbit radiometric calibration is proposed based on the space cryogenic absolute radiometer [10, 11]. Supported by the National Natural Science Foundation of China and the National High-tech R&D Program (863 Program), Changchun Institute of Optics, Fine Mechanics and Physics propose to develop the absolute radiance calibration primary radiometer (ARCPR), and establish in orbit radiometric calibration standard. Based on the ARCPR, the in orbit radiometric calibration method can trace back to SI, and improve calibration accuracy.

The ARCPR is a mechanical cryogenic absolute radiometer, and works at 20 K. According to the electrical substitution principle, all of the measurement parameters can be traced back to SI, and the radiation measurement results can be directly traced to the basic unit of the current (I). The ARCPR has total solar irradiance detectors and high-sensitivity detectors. The sun is used as the calibration optical source, the solar irradiance standard is established by the total solar irradiance detectors, and transferred to other total solar irradiance monitor instruments by synchronous total solar irradiance measurement. Based on the outputs of the solar monochromator, the solar spectrum irradiance standard is established by the high-sensitivity detectors, and transferred to other remote optical sensing instruments by the standard transfer

chain of radiometric calibration. The standard transfer chain consists of integral sphere transfer radiometer, solar diffuse reflector, and earth imaging spectrometer [12]. The in orbit radiometric calibration method based on ARCPR, not only can improve the measurement precision of the radiance source but also can provide the mutual comparison standard for different remote sensors. The comparability and continuity of the different remote sensor are remarkably improved. It is significant to develop ARCPR for the application of remote sensing data scientifically and effectively.

The ground-based cryogenic absolute radiometer generally adopts liquid-helium cooled mode [13–17]. However, the liquid-helium cooled mode cannot satisfy the aerospace application requirements. In order to reduce the volume, and improve the working life, the mechanical refrigeration mode is adopted by ARCPR [18, 19]. However, compared with liquid-helium cooled mode, the mechanical refrigerator has a tremendous thermal noise. Meanwhile, limited by the efficiency of the mechanical refrigeration machine, the working temperature of ARCPR is designed as 20 K. The detector of ARCPR is made of oxygen-free copper. The thermal links in the detector are made of stainless steel. With the temperature increment, the heat capacity of oxygen-free copper is increasing and the heat conductivity of stainless steel is reducing. Thus, compared with 5 K, the difficulty of the 20 K cryogenic detector design is increased [20–24]. Thus, the experimental prototype of ARCPR has been developed for the 20 K cryogenic detector optimisation and the high-stable cryogenic environment establishment. Based on the experimental prototype, the high sensitivity cryogenic detector is designed for satisfying the requirement of the solar spectrum irradiance measurement applications. The investigation results can provide the technical storage for realising the high-accuracy spectrum calibration on satellite of remote sensors in the future.

The development of the experimental prototype is introduced in this paper. The experimental prototype consists of the cryogenic detectors, the mechanical refrigeration machine and the electronics system. In order to establish a high stable thermal environment for the detector, a two-stage temperature controller is developed. Then the thermal characteristics of the detector are experimentally measured for investigating the thermal parameters design. The measurement procedure of optical power is optimised for satisfying

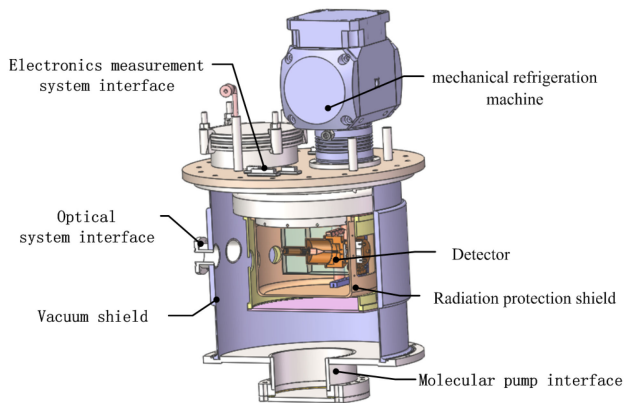


Fig. 1 Design of the ARCPR experimental prototype

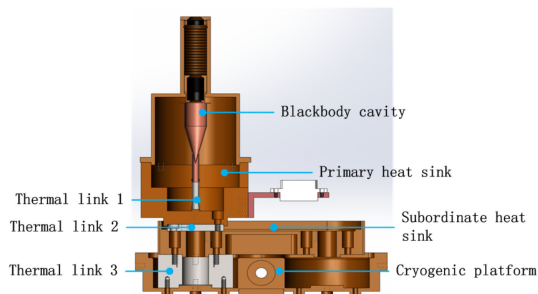


Fig. 2 Sectional view of the detector

the measurement requirements in orbit. The laser power is repeatedly measured, and the uncertainty of ARCPR is analysed.

2 ARCPR experimental prototype design

The experimental prototype is shown in Fig. 1. The height is 550 mm, the width is 300 mm, and the total mass is 30 kg. The rated power of ARCPR is 240 W. The detector is sealed in the vacuum shield ($<10^{-4}$ Pa). The 20 K working temperature is provided by the mechanical refrigeration machine. The test optical source entrances the detector through the optical system interface.

2.1 Detector

As shown in Fig. 2, the detector consists of four components: (i) blackbody cavity, (ii) primary heat sink, (iii) subordinate heat sink and (d) cryogenic platform. The components are both manufactured by oxygen-free copper. The components are, respectively, connected by stainless steel thermal links. The technical route of combining simulation analysis with experimental test is adopted [25]. According to the investigated results, the cavity and the connection structures are designed for improving the sensitivity, as shown in Table 1.

The blackbody cavity is designed according to the effective emissivity simulation results of Dr. Fang [26]. In order to increase the reflection times of the incident light, the blackbody cavity adopts a cylindrical cavity with a cone bottom as shown in Fig. 3. The internal surface of the blackbody cavity is sprayed by the black paint. Experimental measurement results illustrate that the blackbody cavity absorption is 0.999928 ± 0.000006 (1σ) at a wavelength of 632 nm [27]. The incoming optical source is repeatedly reflected and absorbed, and converts to a temperature rise of the blackbody cavity. The electrical power is loaded on the blackbody cavity by the electric heating wire. The electrical power also converts to a temperature rise of the blackbody cavity. According to the electrical substitution principle, when the temperature rise caused by an unknown optical power is reproduced by an equivalent electrical power, the unknown optical power can be determined by precisely measuring the equivalent electrical power [28–30].

2.2 Mechanical refrigeration machine

The Stryn-type pulse tube cryocooler (SPTC) has three advantages: (i) small volume, (ii) little vibration, (iii) long working life. ARCPR adopts SPTC to obtain the cryogenic working environment. The core component of SPTC is the compressor as shown in Fig. 4. The working gas is compressed into liquid and absorbs the heat of the pulse tube. The heat quantity of the cool head is exported by the pulse tube. In order to facilitate the coupling between cool head and the cryogenic detector, SPTC uses a coaxial configuration. The pulse tube and the compressor are combined together in order to reduce the volume. The radiation protection shield is added outside the detector in order to reduce the thermal radiation from room temperature. The experimental prototype uses a liquid-nitrogen storage device to reduce the temperature of the radiation protection shield. The mechanical cooling mode of the radiation protection shield is under developing. The liquid-nitrogen storage device will be replaced by the mechanical cooling device.

SPTC adopts the PID temperature control algorithm. As shown in Fig. 5, the temperature of the detector is reduced by SPTC. The cooling efficiency of SPTC is influenced by the radiation protection shield. When the radiation protection shield temperature is reduced to the lowest, the cooling efficiency of SPTC is the maximum. Thus there is an inflection point in the cooling process. After about 10 h, the cryogenic platform temperature stabilised at the target temperature (21.8 K). The temperature stability of the cryogenic platform is only 13 mK (3σ). Thus, it is necessary to investigate the temperature control system with a higher precision for optimising the environment temperature stability of the blackbody cavity.

2.3 Electronics system

The primary functions of the electronics system are divided as shown in Fig. 6. The computer software of the master computer is developed by LabVIEW. The general-purpose interface bus (GPIB) cables are used to parallel connect the multimeters, including Keysight 34420A, Agilent 34401A, Lake Shore 218, and Keithley 2700. The temperatures of the 20 K temperature field are both measured by the thin film resistance temperature sensors (Cernox-1080). The sensitivity of the Cernox-1080 is -156% ($(dR/R)/(dT/T)$) at 20 K. The measurement range of Cernox-1080 is from 100 mK to 420 K. The temperatures of 80 K temperature field are measured by platinum resistances. The electric heating wires are installed on the blackbody cavity and the heat sinks. The electrical powers are controlled by the embedded system. The shutter is also controlled by the embedded system. The temperature stability of the cryogenic environment is achieved by the temperature control system.

3 Thermal environment establishment

The establishment of the high stable cryogenic environment is the foundation for all the cryogenic material characteristic measurements and the investigation of the detector design. Compared with the liquid-helium cooled mode, the mechanical refrigeration machine of ARCPR has a tremendous thermal noise. In order to establish a high stable thermal environment for the blackbody cavity, a two-stage temperature controller is designed. The switching modulation controller is used to improve the temperature stability of the subordinate heat sink. Based on PI controller, the primary heat sink obtains higher temperature stability, and provides a stable thermal environment for blackbody cavity.

3.1 Temperature controller of the subordinate heat sink

A Cernox-1080 is installed on the subordinate heat sink. The resistance value of the Cernox-1080 is measured by Agilent 34401A, and uploaded to the master computer. Then the subordinate heat sink temperature is obtained by the temperature calibration curve. The temperature measurement accuracy is 0.2 mK (3σ). In order to rapidly restrain the thermal noise, the

Table 1 Optimized thermal parameters of the cryogenic detector

Cryogenic detector components	Mass, g	Heat capacity, J/K		Thermal resistance, K/W	
		20 K	25 K	20 K	25 K
blackbody cavity	3.9	0.02925	0.06054		
thermal link 1	0.5			3000	2300
primary heat sink	478	3.585	7.409		
thermal link 2	20			23.5	18.0
subordinate heat sink	350	2.625	5.425		
thermal link 3	171			8.7	6.7
cryogenic platform	900	6.75	13.95		

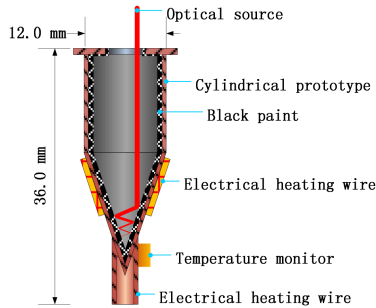


Fig. 3 Structure of the blackbody cavity

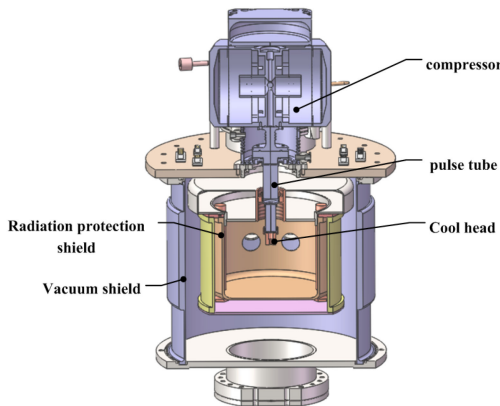


Fig. 4 SPTC structure

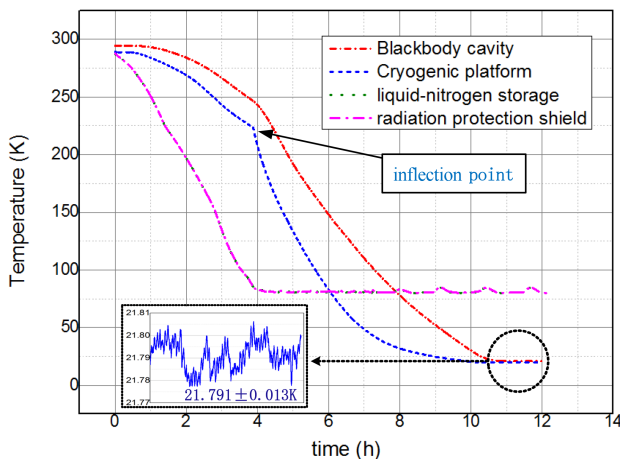


Fig. 5 Cooling process and the temperature stability of the SPTC

temperature controller of the subordinate heat sink needs rapid adjustment capability. The switching modulation algorithm is designed as shown in Fig. 7. The input of the switching modulation algorithm is the temperature difference ($E_{SHS}(n)$), which is depicted as

$$E_{SHS}(n) = T_{0SHS} - T_{SHS} \quad (1)$$

where T_{0SHS} is the target temperature, T_{SHS} is the real-time temperature of the subordinate heat sink. As a first-order inertial system, the real-time temperature of the subordinate heat sink has hysteresis quality. The switching modulation algorithm can suppress the overshoot by judging the temperature difference variety ($\Delta E_{SHS}(n)$), which is expressed as

$$\Delta E_{SHS}(n) = E_{SHS}(n) - E_{SHS}(n - 1) \quad (2)$$

As shown in Fig. 7, the output of the temperature control algorithm of switching modulation is electrical heating power ($P(n)$). When $|E_{SHS}(n)|$ is bigger than 2 mK, $P(n)$ is only depended on $E_{SHS}(n)$. When $|E_{SHS}(n)|$ is smaller than 2 mK, $P(n)$ is depended on $E_{SHS}(n)$ and $\Delta E_{SHS}(n)$.

According to the temperature variation, the switching modulation algorithm adjusts the electrical heating power of the subordinate heat sink. The cryogenic experiment results illustrate that when loaded an average electrical heating power of 30.33 mW, the subordinate heat sink temperature stabilised at 22.255 ± 0.002 K (3σ). The environment temperature stability is improved from 13 to 2 mK.

3.2 Temperature controller of the primary heat sink

The temperature sensor (Cernox-1080) is installed on the primary heat sink. The resistance value of the Cernox-1080 is measured by Agilent 3458A, and uploaded to the temperature control computer. Then the primary heat sink temperature is obtained by the temperature calibration curve. The temperature measurement accuracy is 0.03 mK (3σ). Based on the proportional integral (PI) algorithm, the temperature controller of the primary heat sink is developed. The transfer function ($C(s)$) of PI algorithm is expressed as

$$C(s) = \frac{P(s)}{E(s)} = K_P \left(1 + \frac{I}{s} \right) \quad (3)$$

where K_P is the proportional factor, I is the integral factor, $P(s)$ is the output electrical power, $E(s)$ is the input temperature difference, which is depicted as

$$E(s) = T_{0PHS} - T_{PHS} \quad (4)$$

here T_{0PHS} is the target temperature, T_{PHS} is the real-time temperature of the primary heat sink. The control factors (K_P and I) are determined by the mathematical model of the primary heat sink.

When the subordinate heat sink temperature is stable, a constant electrical heating power is loaded on the primary heat sink. Then the mathematical model of the primary heat sink is obtained by fitting the temperature response curve. The mathematical model of the primary heat sink is expressed as

$$H(s) = \frac{0.0001239}{s + 0.002353} \quad (5)$$

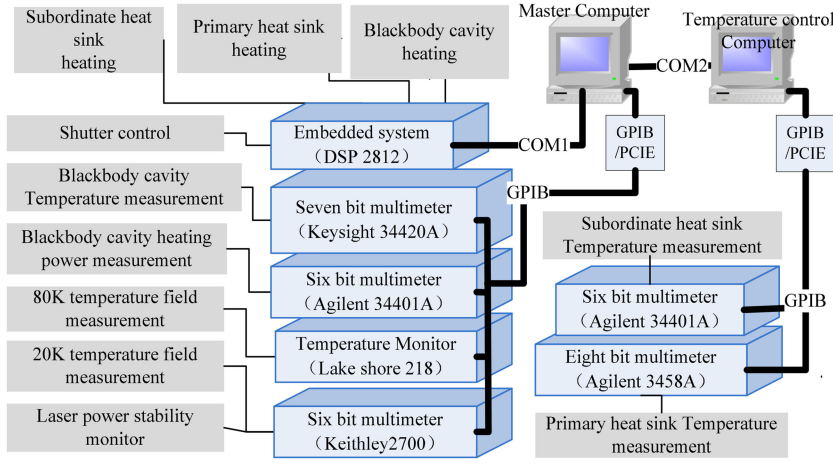


Fig. 6 Electronics system of ARCPR

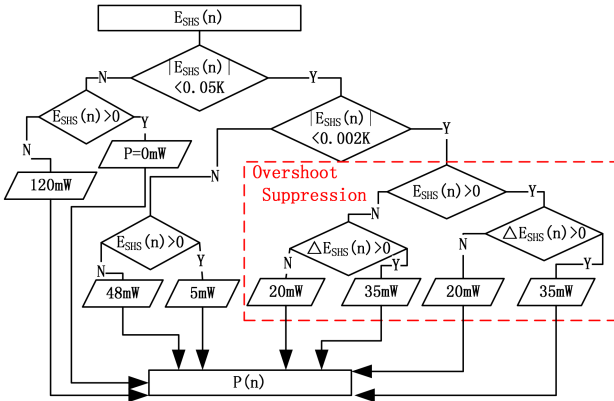


Fig. 7 Temperature control algorithm of switching modulation

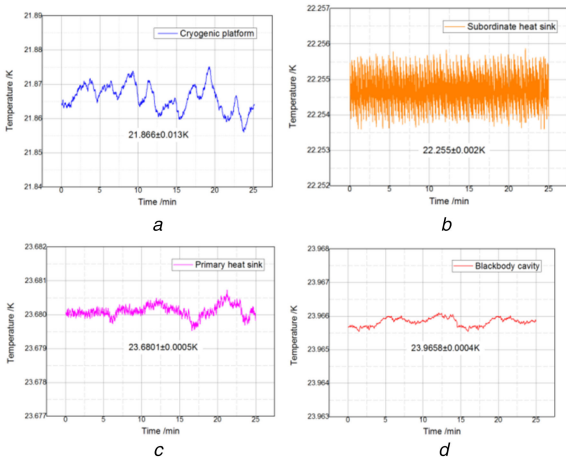


Fig. 8 Temperature stability of the detector components (a) Cryogenic platform, (b) Subordinate heat sink, (c) Primary heat sink, (d) Blackbody cavity

Based on the mathematical model, the control factors (KP and I) are optimised by Matlab Simulink. When $K_p = 289.933$ and $I = 0.00354176$, the phase margin is 87.6° , the gain margin is 40.9 dB.

According to the temperature variation, the PI algorithm adjusts the electrical heating power of the primary heat sink. The cryogenic experiment results illustrate that under the action of the PI algorithm, the primary heat sink temperature stabilised at 23.9658 ± 0.0005 K (3σ). Thus, the environment temperature stability is improved from 2.0 to 0.5 mK.

3.3 Establishment of the stable cryogenic environment

As shown in Fig. 8, the cryogenic platform temperature is reduced to 21.866 ± 0.013 K by SPTC. The thermal noise of the cryogenic

platform is compensated by the temperature controller of subordinate heat sink. The primary heat sink achieves 0.5 mK temperature stability by PI controller. Based on the high stable cryogenic environment, the detector design is experimentally investigated.

4 Thermal characteristics of detector

According to the one-dimensional thermal model, the thermal equilibrium equation of the blackbody cavity is expressed as

$$C \frac{dT_C(t)}{dt} + \frac{1}{R} [T_C(t) - T_{PHS}] = P + P_S. \quad (6)$$

where $T_C(t)$ is the temperature dynamic response of the blackbody cavity, T_{PHS} is the primary heat sink temperature, C is the heat capacity, R is the heat resistance, P is the heating power of the blackbody cavity, P_S is the thermal radiation noise. Solving (6), $T_C(t)$ is depicted as

$$T_C(t) = T_{PHS} + T_2 + (T_1 - T_2)e^{-(t/\tau)}. \quad (7)$$

where T_1 is the initial temperature difference, τ is the thermal time constant, which represents the temperature response speed. τ is expressed as

$$\tau = CR. \quad (8)$$

T_2 is the equilibrium temperature difference, which is depicted as

$$T_2 = (P + P_S)R. \quad (9)$$

As time $t \rightarrow \infty$, $T_C(\infty)$ approaches T_2 :

$$\begin{aligned} T_C(\infty) &= \lim_{t \rightarrow \infty} T_C(t) \\ &= \lim_{t \rightarrow \infty} [T_2 + (T_1 - T_2)e^{-(t/\tau)}] \\ &= T_2. \end{aligned} \quad (10)$$

In practical application, $T_C(10\tau)$ is approximately equal to T_2 , as follows:

$$\begin{aligned} T_C(10\tau) &= T_2 + (T_1 - T_2)e^{-(10\tau/\tau)} \\ &= 0.99995T_2 + 0.00005T_1 \\ &\simeq T_2. \end{aligned} \quad (11)$$

The relationship between T_2 and P can be described by linear fitting, which is expressed as

$$T_2 = f(P). \quad (12)$$

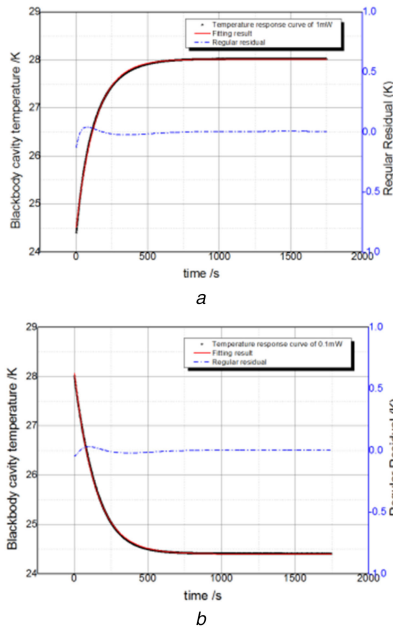


Fig. 9 Temperature response fitting result of the blackbody cavity
(a) Heating process, (b) Cooling process

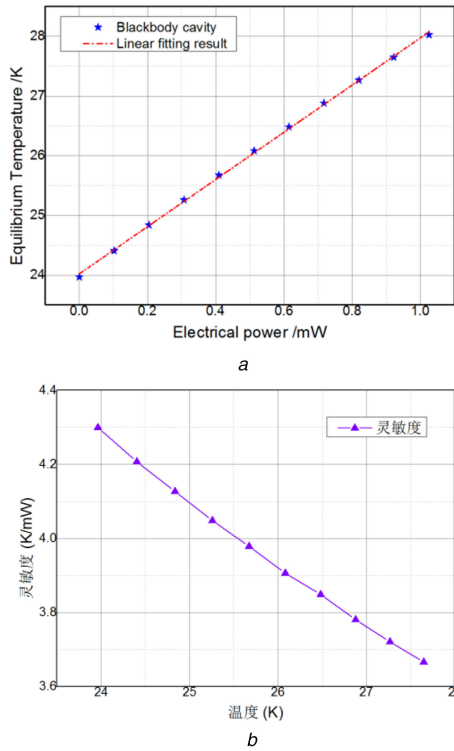


Fig. 10 Sensitivity fitting result
(a) Sensitivity between 24 and 28 K, (b) Sensitivity at different working temperature

The gradient of the mathematical model is called the sensitivity (S), which is depicted as

$$S = df(T_2)/dP. \quad (13)$$

The thermal characteristics of the detector are obtained by thermoelectric experiments.

4.1 Thermal time constant

When heated by a constant electrical power, the blackbody cavity temperature arrives at an equilibrium status from initial status. The temperature response curves are measured by temperature monitor (Cernox-1080). Based on the least square algorithm, the temperature response curves are fitted as shown in Fig. 9. Then, the

thermal time constant is obtained. The experimental results illustrate that the thermal time constant is $137 \pm 2 \text{ s}(3\sigma)$ at 25 K. According to Table 1, the design value of the thermal time constant is 139 s at 25 K. The design and measured values of thermal time constant are agreed well.

The experimental results also illustrate that the thermal time constants are $134 \pm 2 \text{ s}(3\sigma)$ and $143 \pm 2 \text{ s}(3\sigma)$, respectively, at 24.5 and 28 K. According to (8), the difference between the thermal time constants comes from the characteristic change of the cryogenic materials. The heat capacity of the oxygen-free copper is reducing with the temperature decrease. Meanwhile, the heat resistance of stainless steel increases. Experimental results illustrate that when the blackbody cavity temperature is increased from 24.5 to 28 K, the thermal time constant increases 7%.

4.2 Sensitivity

The blackbody cavity is heated by electrical powers ($P(x)$), and arrives equilibrium status. $P(x)$ is gradually increased from 0.1 to 1.0 mW, and the increment is 0.1 mW. The equilibrium temperatures ($T_2(x)$) are obtained and measured. The relationship between $P(x)$ and $T_2(x)$ is obtained by linear fitting as shown in Fig. 10a. Experimental results illustrate that within the temperature range between 24 and 28 K, the sensitivity is 3.9526 K/mW. As shown in Fig. 10b, the sensitivities at different working temperature are calculated by two adjacent equilibrium temperatures. The sensitivity is descending with the temperature rise. When the working temperature is rising 1 K, the sensitivity is descending 4.3%.

5 Optical power measurements

Due to the long thermal time constant (about 2 min) of the blackbody cavity, the measurements of optical power with ARCPR are very time consuming. When adopts the traditional measurement method of the two electric calibrations [31], one optical power measurement period needs 60 min. The traditional measurement method cannot satisfy the requirement of space applications. An optimised method is proposed for shortening the measurement period.

5.1 Measurement procedure

Before optical observation, the blackbody cavity is preheated by an electrical heating power (P_H). The optimised method consists of optical observation and electric calibration, as shown in Fig. 11.

At the beginning of optical observation, the electric power is cut off and the shutter is opened. According to the cavity temperature change ($T_C(t_1)$ and $T_C(t_2)$), the equilibrium temperature (T_0) can be obtained, which is depicted as

$$T_0 = \frac{T_C(t_1) - T_C(t_2) \times \exp(-(t_1 - t_2)/\tau)}{1 - \exp(-(t_1 - t_2)/\tau)} \quad (14)$$

The optical power (P_O) can be approximately obtained by sensitivity. Then the difference between P_H and P_O can be calculated, and compensated by the electric power (P_{OE}). Under the combined heating of P_O and P_{OE} , the equilibrium status of the blackbody cavity is maintained. Therefore, the optical observation time is shortened to 12 min from 20 min. The equilibrium temperature (T_{01}) is obtained by optical observation.

The shutter is closed during electric calibration. The blackbody cavity is only heated by the electrical calibration power (P_E), which is calculated by T_{01} . The equilibrium temperature (T_{02}) is obtained by optical observation. P_O can be calculated as

$$P_O = \eta[P_E - P_{OE} - S \times (T_{02} - T_{01})]/\alpha\beta + P_S \quad (15)$$

where η is the non-equivalence between the optical and electrical heating, α is the absorption of the blackbody cavity, β is the transmissivity of the incidence window, P_S is the stray light power.

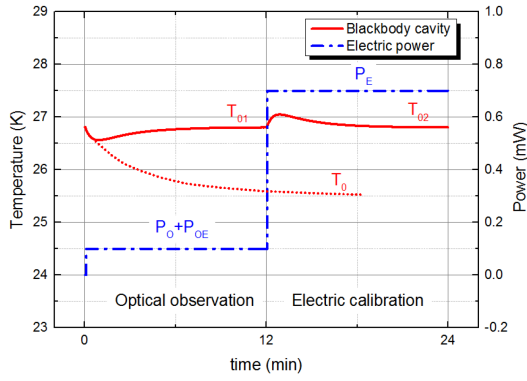


Fig. 11 Measurement method design of ARCPR

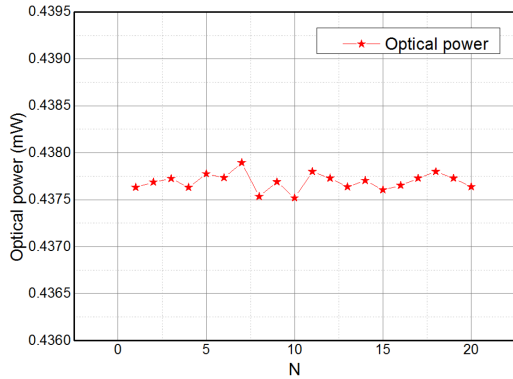


Fig. 12 Laser power repeatedly measurement result

Table 2 Uncertainty analysis

Components	Correction value	Uncertainty, ppm
non-equivalence	1	5
cavity absorption	0.999928	6
transmissivity	0.99947	130
standard resistant	—	50
cavity temperature	—	20
heating voltage	—	45
stray light power	11 μ W	80
total	—	210

The measurement period is shortened to 24 min by the optimised method.

5.2 Measurement result and uncertainty analysis

In order to evaluate the precision of the ARCPR, the high stable optical path is built. Due to the spectral coverage of the blackbody cavity is 300–2500 nm, the laser power ($\lambda = 632$ nm) is used as the optical source. The stability of the optical source is improved from 0.1 to 0.01% by the power stabiliser. The output of the power stabiliser is used as the test optical source. At the same condition, the test optical source is repeatedly measured by ARCPR. As shown in Fig. 12, the repeatedly measurement result is 0.4377 ± 0.0001 mW (1σ). The relative accuracy is 0.02%.

The sensitivity between the equilibrium temperatures can be calculated by linear fit, as follows:

$$S = \frac{P_H - P_L}{T_H - T_L} \quad (16)$$

where P_H is the high electrical power, P_L is the low electrical power. T_H and T_L are corresponding equilibrium temperatures.

The electrical heater is parallel connected with a standard resistant (R). Pass through measuring the voltages of the electrical heater (V_X) and standard resistant (V_{RX}), the electrical powers are obtained and calculated as

$$P_H = \frac{V_H V_{RH}}{R} \quad (17)$$

$$P_L = \frac{V_L V_{RL}}{R} \quad (18)$$

$$P_E = \frac{V_E V_{RE}}{R} \quad (19)$$

$$P_{OE} = \frac{V_{OE} V_{ROE}}{R} \quad (20)$$

where V_H , V_L , V_E , V_{OE} are the voltage of the electrical heater, V_{RH} , V_{RL} , V_{RE} , V_{ROE} are the voltage of the standard resistant, R is the resistance of the standard resistant.

Then, according to (15)–(20), the mathematical model of optical power measurement is depicted as

$$P_O = P_S + \frac{\eta}{\alpha\beta R} \left[V_E V_{RE} - V_{OE} V_{ROE} - \frac{(V_H V_{RH} - V_L V_{RL})(T_{O2} - T_{O1})}{T_H - T_L} \right] \quad (21)$$

Thus, the relative standard uncertainty (u_r) of ARCPR is depicted as

$$u_r^2 = \left[\frac{u(P_O)}{P_O} \right]^2 = \left[\frac{u(\eta)}{\eta} \right]^2 + \left[\frac{u(\alpha)}{\alpha} \right]^2 + \left[\frac{u(\beta)}{\beta} \right]^2 + \left[\frac{u(R)}{R} \right]^2 + 2 \left[\frac{u(T_H)}{T_H} \right]^2 + 2 \left[\frac{u(T_L)}{T_L} \right]^2 + \left[\frac{u(T_{O1})}{T_{O1}} \right]^2 + \left[\frac{u(T_{O2})}{T_{O2}} \right]^2 + \left[\frac{u(V_H)}{V_H} \right]^2 + \left[\frac{u(V_L)}{V_L} \right]^2 + \left[\frac{u(V_{RH})}{V_{RH}} \right]^2 + \left[\frac{u(V_{RL})}{V_{RL}} \right]^2 + \left[\frac{u(V_E)}{V_E} \right]^2 + \left[\frac{u(V_{OE})}{V_{OE}} \right]^2 + \left[\frac{u(V_{RE})}{V_{RE}} \right]^2 + \left[\frac{u(V_{ROE})}{V_{ROE}} \right]^2 + \left[\frac{u(P_S)}{P_O} \right]^2 \quad (22)$$

The analysis result of uncertainty components is shown in Table 2. The electrical heater is embedded inside the blackbody cavity. Pass through the finite element analysis, the non-equivalence is approximated to 1, and the relative uncertainty of η is 5 ppm.

Base on the substitution method, the cavity absorbance measure equipment is established, the relative uncertainty of α is 6 ppm [32].

When the optical path is locked, the test optical source is measured on both sides of the incidence window. The transmissivity of the incidence window is obtained, and the relative uncertainty of β is 130 ppm.

The standard resistant is measured by Agilent 34401A. According to the technical manual and experimental results, the relative uncertainty of R is 50 ppm.

The cavity temperature is measured by Keysight 34420A. The measurement accuracy of cavity temperature is determined by the accuracy of measurement equipment and cryogenic environment stability. According to the technical manual and experimental results, the relative uncertainty of T is 20 ppm.

The voltage is measured by Agilent 34401A, According to the technical manual and experimental results, the relative uncertainty of V is 45 ppm.

The measurement equipment of stray light power is established. The experimental and analyse results illustrate that the relative uncertainty of P_S is 80 ppm.

In summary, the relative uncertainty of ARCPR is 210 ppm.

6 Conclusions

In order to investigate the optimisation design of detector, the experimental prototype of ARCPR is established. The experimental

prototype is a mechanical cryogenic absolute radiometer, and consists of the detector, the mechanical refrigeration machine and the electronics system. This paper introduces the establishment of the thermal environment. Then the design of the detector is experimentally investigated.

The cryogenic environment is obtained by SPTC. The temperature of the cryogenic platform is reduced to 21.866 K. Meanwhile, the cryogenic platform has a 16 mK (P-P) thermal noise. The two-stage temperature controller is developed. The cryogenic environment temperature is stable at 23.9658 ± 0.0005 K (3σ). Due to the compensation of the thermal noise, the blackbody cavity temperature measurement accuracy is improved to 146 ppm.

The thermal model of cavity temperature is obtained by thermal equilibrium equation. According to the theoretical analysis and experimental test, the temperature response of the cryogenic detector has a single exponential form. The characteristics of the blackbody cavity are experimentally measured. The experimental results illustrate that the cryogenic detector sensitivity is improved to 3.9526 K/mW by the heat transfer structure optimisation. The sensitivity is descending with the temperature rise. When the working temperature is rising 1 K, the sensitivity is descending 4.3%. The experimental results also illustrate that the thermal time constant is 134 ± 2 s (3σ) at 24.5 K. When increased from 24.5 to 28 K, the thermal time constant of the blackbody cavity increases 7%.

An optimised method is proposed for satisfying the requirement of space applications. In order to evaluate the precision of experimental prototype, the optical power is repeatedly measured. The repeatedly measurement result is 0.4377 ± 0.0001 mW ($\lambda = 632$ nm). The uncertainty components are analysed. The experimental prototype achieves a relative standard uncertainty of 210 ppm. Therefore, it is significant to investigate the experimental characteristics of the experimental prototype. The investigation results provide the theoretical and experimental basis for the ARCPR design.

7 Acknowledgments

The authors thank numerous staffs in Changchun Institute of Optics, Fine Mechanics and Physics, Chinese Academy of Sciences, including Song Baoqi, Jia Ruidong, Zheng Siqiao, Wu Duo and many others. The authors are grateful to Yu Bingxi, former project leader of SIAR, for his great contributions and guidance. The authors also thank the referee for generous help and good comments. This work was supported by the National Key R&D Program of China (grant nos. 2018YFB0504600, 2018YFB0504603), the National Natural Science Foundation of China (NSFC) (grant nos. 41474161 and 41227003) and the National High-tech R&D Program(863 Program) (grant no. 2015AA123703).

8 References

- [1] Willson, R.C.: 'ACRIM3 and the total solar irradiance database', *Astrophys. Space Sci.*, 2014, **352**, pp. 341–352
- [2] Menegotto, T., da Silva, T.F., Simoes, M.: 'Realization of optical power scale based on cryogenic radiometry and trap detectors', *IEEE Trans. Instrum. Meas.*, 2015, **64**, (6), pp. 1702–1708
- [3] Xiong, J., Cao, C., Chander, G.: 'An overview of sensor calibration inter-comparison and applications', *Front. Earth Sci. China*, 2010, **4**, (2), pp. 237–252
- [4] Cooksey, C., Datla, R.: 'Workshop on bridging satellite climate data gaps', *J. Res. Natl. Inst. Stand. Technol.*, 2011, **116**, (1), pp. 505–516
- [5] Eplee, R.E.Jr., Turpie, K.R., Meister, G., et al.: 'On-orbit calibration of the Suomi national polar-orbiting partnership visible infrared imaging radiometer suite for ocean color applications', *Appl. Opt.*, 2015, **54**, (8), pp. 1984–2006
- [6] Kopp, G., Lawrence, G.: 'The total irradiance monitor (TIM): instrument design', *Sol. Phys.*, 2005, **230**, pp. 91–109
- [7] Gergor, H., Julian, G., Saulius, N., et al.: 'Traceability of solar UV measurements using the Qasum reference spectroradiometer', *Appl. Opt.*, 2016, **55**, (26), pp. 7265–7275
- [8] Willson, R.C.: 'Active cavity radiometer type IV', *Appl. Opt.*, 1979, **18**, pp. 179–188
- [9] Walter, B., Fehlmann, A., Finsterle, W., et al.: 'Spectrally integrated window transmittance measurements for a cryogenic solar absolute radiometer', *Metrologia*, 2014, **51**, pp. 344–349
- [10] Martin, J.E., Fox, N.P.: 'Cryogenic solar absolute radiometer (CSAR)', *Metrologia*, 1993, **30**, pp. 305–308
- [11] Fox, N., Aiken, J., Barnett, J.J., et al.: 'Traceable radiometry underpinning terrestrial and helio-studies (TRUTHS)'. Proc. of SPIE, 2003, vol. **4881**, pp. 395–406
- [12] Yupeng, W., Xiuqing, H., Hongrui, W., et al.: 'Standard transfer chain for radiometric calibration of optical sensing instruments with traceability in solar reflective bands', *Opt. Precis. Eng.*, 2015, **23**, (7), pp. 1807–1812
- [13] Hoyt, C.C., Foukal, P.V.: 'Cryogenic radiometers and their application to metrology', *Metrologia*, 1991, **28**, pp. 163–167
- [14] Pearson, D.A., Zhang, A.M.: 'Thermal-electrical modeling of absolute cryogenic radiometers', *Cryogenics*, 1999, **39**, pp. 299–309
- [15] Fox, N., Haycocks, P., Martin, J., et al.: 'A mechanically cooled portable cryogenic radiometer', *Metrologia*, 1995, **32**, pp. 581–584
- [16] Morozova, S.P., Konovodchenko, V.A., Sapritsky, V.I., et al.: 'An absolute cryogenic radiometer for laser calibration and characterization of photodetectors', *Metrologia*, 1995, **32**, pp. 557–560
- [17] Tomlin, N.A., Lehman, J.H.: 'Carbon nanotube electrical-substitution cryogenic radiometer: initial results', *Opt. Lett.*, 2013, **38**, (2), pp. 175–177
- [18] Dykema, J.A., Anderson, J.G.: 'A methodology for obtaining on-orbit SI-traceable spectral radiance measurements in the thermal infrared', *Metrologia*, 2006, **43**, pp. 287–293
- [19] Fox, N., Weiss, K., Schmutz, W., et al.: 'Accurate radiometry from space: an essential tool for climate studies', *Philos. Trans. R. Soc. A*, 2011, **369**, pp. 4028–4063
- [20] Goebel, R., Pello, R., Kohler, R., et al.: 'Comparison of the BIPM cryogenic radiometer with a mechanically cooled cryogenic radiometer from the NPL', *Metrologia*, 1996, **33**, pp. 177–179
- [21] Houston, J.M., Rice, J.P.: 'NIST reference cryogenic radiometer designed for versatile performance', *Metrologia*, 2006, **43**, pp. 31–35
- [22] Martin, J.E., Fox, N.P., Key, P.J.: 'A cryogenic radiometer for absolute radiometric measurements', *Metrologia*, 1985, **21**, pp. 147–155
- [23] Carr, S.M., Woods, S.L., Jung, T.M.: 'Experimental measurement and noise analysis of a cryogenic radiometer', *Rev. Sci. Instrum.*, 2014, **85**, p. 075105
- [24] Willson, R.C.: 'Active cavity radiometer', *Appl. Opt.*, 1973, **12**, pp. 810–817
- [25] Xiao, T., Wei, F., Yang, L., et al.: 'Thermal characteristic analysis of heat sink in absolute radiometer', *Acta Opt. Sin.*, 2016, **36**, (10), p. 1012004
- [26] Fang, Q., Fang, W., Wang, Y., et al.: 'New shape of blackbody cavity: conical generatrix with an inclined bottom', *Opt. Eng.*, 2012, **51**, (8), p. 086401
- [27] Xiaolong, Y., Zhenling, Y., Xin, Y., et al.: 'Absorptance measurement for sloping bottom cavity of cryogenic radiometer', *Opt. Precis. Eng.*, 2015, **23**, (10), pp. 1–7
- [28] Yang, Z., Fang, W., Luo, Y., et al.: 'Experimental characterization and correction of non-equivalence of solar irradiance absolute radiometer', *Chin. Opt. Lett.*, 2014, **12**, (10), p. 101202
- [29] Fang, W., Wang, H., Li, H., et al.: 'Total solar irradiance monitor for Chinese FY-3A and FY-3B satellites-instrument design', *Sol. Phys.*, 2014, **289**, pp. 4711–4726
- [30] Wang, H., Li, H., Qi, J., et al.: 'Total solar irradiance monitor for the FY-3B satellite-space experiments and primary data corrections', *Sol. Phys.*, 2015, **290**, pp. 645–655
- [31] Gentile, T.R., Houston, J.M., Hardis, J.E., et al.: 'National Institute of Standards and Technology high-accuracy cryogenic radiometer', *Appl. Opt.*, 1996, **35**, (7), pp. 1056–1068
- [32] Xiaolong, Y., Wei, F., Yang, L., et al.: 'Correction of cavity absorptance measure method for cryogenic radiometer', *IET Sci. Meas. Technol.*, 2016, **10**, (6), pp. 564–569